Anion velocity imaging study of the dissociative electron attachment to $CFCl_3$

Xian-Jin Zeng,[1] Lei Xia,[1] Hong-Kai Li,[1] Kai-Chung Lau,[2] and Shan Xi Tian[1,*]

[1]*Hefei National Laboratory for Physical Sciences at the Microscale and Department of Chemical Physics, University of Science and Technology of China, 96 Jinzhai Road, Hefei, Anhui 230026, China*

[2]*Department of Biology and Chemistry, City University of Hong Kong, 83 Tat Chee Avenue, Kowloon, Hong Kong, China*

(Received 14 December 2012; published 29 January 2013)

Time-sliced velocity imaging experiments have been performed for the low-energy electron dissociative attachment to $CFCl_3$ in the gas phase. The time-sliced velocity images of the F^- anionic fragment, recorded at different electron attachment energies (2.0–7.0 eV), indicate image pattern evolutions. The angular and kinetic energy distributions of the F^- fragment are interpreted with two shape-resonant states of $CFCl_3{}^-$ and thermochemistry calculations for dissociation thresholds. The dramatic reduction of the F^- kinetic energy observed at higher attachment energies is possibly due to two-body dissociation with an electronically excited state of CCl_3 ($^2A''$) or three-body dissociations.

DOI: 10.1103/PhysRevA.87.012711 PACS number(s): 34.80.Ht

I. INTRODUCTION

The dynamics of electron collisions with halogenated methane molecules is a key in several industrial and environmental applications [1]. At low electron energy (below the ionization thresholds of the halogenated methanes), dissociative electron attachment (DEA) is an efficient pathway for the decomposition of these molecules [1]. Thus the electron-molecule resonant system as the dissociative precursor, together with its DEA products (anionic and neutral fragments), receives much attention in many fields of physics and chemistry. Electron transmission [2,3] and anion mass [4,5] spectroscopy provides information about the energy position of an electron-molecule-resonant state formed in the vertical attachment and the production efficiencies of various anionic fragments. Although the kinetic energies of the anionic fragments can be obtained by using linear time-of-flight techniques in anion mass spectroscopy experiments [4,5], the angular distributions are not available. Toward an understanding of the complete DEA dynamics, the momentum distributions (including the kinetic energy and angular distributions) of the fragments are necessary. This has benefited from recent experimental developments by employing the anion velocity imaging technique [6–9].

For trichlorofluoromethane ($CFCl_3$), as a member of the freon molecule family, collisions with low-energy electron and DEA processes have been widely investigated [2–6,10–13]. Three resonant states of the transient anion $CFCl_3{}^-$ have been observed and assigned with σ^*(C-Cl), σ^*(C-Cl), and σ^*(C-F) [3], on the basis of the prediction of the electron captures into the unoccupied valence orbitals a_1 [σ^*(C-Cl)], e [σ^*(C-Cl)], and a_1 [σ^*(C-F)] of the neutral molecule $CFCl_3$ (see Ref. [11]). The multireference configuration interaction (MRCI) calculation was performed to predict the potential energy curves of $CFCl_3{}^-$ at low-lying resonant states [14], but those curves were unreliable in physics because the electron autodetachment by coupling with the electron continuum background was ignored in the quantum chemistry calculations. Four anionic fragments, Cl^-, F^-, $Cl_2{}^-$, and $CCl_3{}^-$, were detected in the anion mass spectra, while the highest product efficiency of Cl^- was found at near-zero electron attachment energy and the productions of $Cl_2{}^-$ and $CCl_3{}^-$ were quite low [4,5]. The asymptote of the dissociative channel $CFCl_3^- \rightarrow CFCl_2 + Cl^-$ lies below the ground state of the neutral molecule $CFCl_3$, leading to the onset at 0 eV in the Cl^- efficiency curve [4,5]. Since the total excess energy of this dissociation is small, the kinetic energy of Cl^- should be too small to explore the related dissociation dynamics by using the anion velocity imaging technique. In this work, we carried out the anion velocity imaging studies for the DEA process with the product F^-. The electron attachment energy range investigated here covered the main broad peak (1.5–4.5 eV [4,5]) and a weak peak around 7.0 eV [5] that were observed in the F^- production curves. According to the symmetries of the anion images, the parity of the resonant state involved in the DEA can be determined [8,9,15]. Previous experimental studies only focused on the resonant states at low energies (less than 5.0 eV), and the weak peak at 7.0 eV of the F^- product [5] was not assigned or clarified. Furthermore, there is still no theoretical work using more sophisticated quantum scattering methods to elucidate the existence of various resonant states of $CFCl_3{}^-$. Therefore, the present work meets this demand and provides much more dynamics information about the DEA process of this molecule.

II. EXPERIMENTAL METHODS AND COMPUTATIONS

The DEA experiments for the gas-phase molecule $CFCl_3$ were done at the selected electron attachment energies, 2.0, 2.5, 3.0, 3.5, 4.0, and 7.0 eV, by using our anion velocity imaging apparatus. The details about this apparatus can be found in Ref. [16]. Briefly, an effusive molecular beam of the sample (along the y axis) was perpendicular to the pulsed electron beam (along the x axis), which was emitted from a homemade electron gun and collimated with the homogenous magnetic field produced by a pair of Helmholtz coils. The F^- ions produced via the DEA process (the other source, e.g., the ion-pair dissociation $e^- + CFCl_3 \rightarrow F^- + CCl_3^+ + e'^-$ can be ruled out due to its higher energetic threshold ca. 10 eV [12]) were periodically pushed out of the reaction area and then

*Corresponding author: sxtian@ustc.edu.cn.

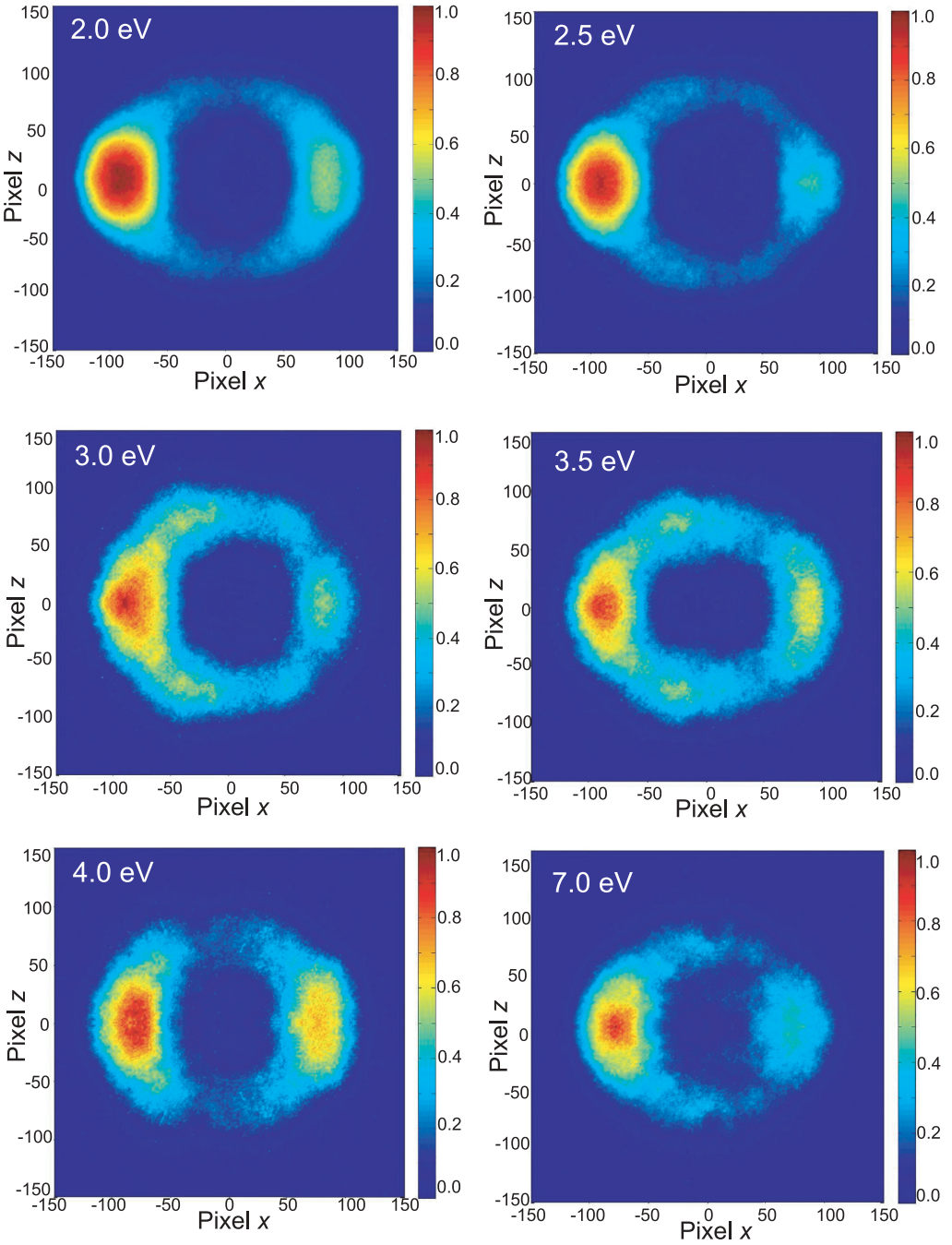

FIG. 1. (Color online) Sliced velocity images of F^- fragment at the different electron attachment energies. The electron incident direction is from left to right and through the center ($z = 0$). The anion intensities of the images are normalized, respectively.

allowed to pass through the time-of-flight tube (along the y axis). The F^- ions that were produced in one electron pulse expanded to form a Newton sphere by the space and velocity focusing [16]. The three-dimensional momentum distributions of the F^- ions were detected with a triplet set of microchannel plates and a phosphor screen. Each time-sliced image of F^- ions, i.e., the central sliced sheet (in the x-z plane) of the Newton sphere, was recorded with a charge-coupled device camera and by the application of a narrow time-gate voltage pulse (width $\sim$ 45 ns) on the last microchannel plate. The velocity values derived from the image were calibrated with the experimental data available in the literatures [8,9,16].

Since the neutral fragments were not detected and the dissociation paths into the F^- ion accompanying the different neutral fragments cannot be identified directly from the experiments, thermochemistry calculations for the energetic thresholds of the possible dissociation channels were performed. The structures of $CFCl_3$ and the fragmented products were optimized at the coupled-cluster theory, i.e., CCSD(T)/aug-cc-pV(T + d)Z level. Based on the optimized structures, single-point valence energy calculations were then carried out at the CCSD(T)/aug-cc-pV(5 + d)Z level [17]. The core-valence energy at the CCSD(T)/aug-cc-pwCVTZ level [18] was included to recover 2s plus 2p (chlorine) and 1s

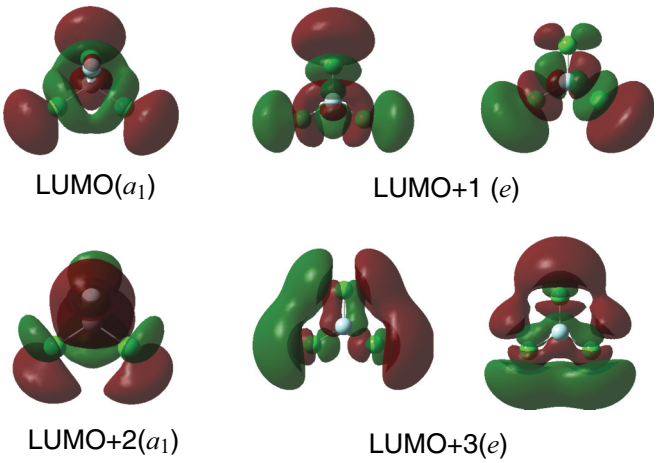

FIG. 2. (Color online) Electron density maps of four low-lying virtual molecular orbitals of $CFCl_3$.Their chemical bonding characters can be easily viewed in different colors.

(fluorine and carbon) electronic correlations in the dissociation process. The relativistic effect was computed using the spin-free, one-electron Douglas-Kroll-Hess (DKH) Hamiltonian [19]. These calculations were done with the DKH-contracted aug-cc-pVTZ-DK basis sets [20] at the CCSD(T) level. Based on the single-point energy at the CCSD(T)/cc-pV(5 + d)Z level together with the core-valence electronic correlation, relativistic effect, and the zero-point energy correction [at the CCSD(T)/aug-cc-pV(T + d)Z level], the threshold energies for the various dissociation channels were obtained. All single-point energy calculations, vibrational frequency calculations, and correlation contributions were performed using the MOLPRO 2010.1 suite of programs [21].

III. RESULTS AND DISCUSSION

Figure 1 shows the time-sliced images of F^- at six different electron attachment energies. The first five energies are around the main peak of F^- centered at ca. 3.2 eV (see the upper panel in Fig. 9 of Ref. [4] and Fig. 2 of Ref. [5]), while the last one corresponds to the energy position of the weak peak observed in Fig. 2 of Ref. [5]. In Fig. 1, the direction of the incident electron is from left to right and through the center of the distribution. The zero degree angle of θ is at the central-right end ($z = 0$ au) in each image. In general, the scattering along the electron beam and the backward reaction is predominant. In the electron attachment energy range of 2.0–4.0 eV, the forward distributions are enhanced continuously with increasing attachment energy. One can also observe other changes of the F^- distribution perpendicular to the electron beam. At 7.0 eV, the forward distribution is reduced dramatically with respect to that observed at 4.0 eV. Besides the reduction of the general image intensity at 7.0 eV, the image size is also smaller, indicating the smaller velocity values of the F^- ions. Therefore, the DEA process at 7.0 eV should be completely different from that at lower electron energies. We will discuss this issue in the following text.

In the previous studies, the resonant state around 3.62 [3] or 4.0 eV [11] was proposed according to the total cross sections of electron transmission experiments; while the F^- production curve indicated a peak at a lower electron energy ca. 3.2 eV [4, 5]. The authors consistently assigned this state formed via the electron capture into the second lowest unoccupied molecular orbital (LUMO + 2) a_1 of the neutral $CFCl_3$. As shown in Fig. 2, the electron density populations of the LUMO and its next three higher MOs are plotted. These virtual orbitals show typical characters as antibond σ^*(C-Cl) [LUMO, a_1], σ^*(C-Cl) [degenerate orbital LUMO + 1, e], σ^*(C-F) [LUMO + 2, a_1], and lone-pair p*(Cl) [degenerate orbital LUMO + 3, e. In agreement with the previous conclusion [3–5,11], the $^2A_1$ resonant state formed via the electron capture into the LUMO + 2 (a_1) should be responsible for the DEA processes that are shown as the images at 2.0, 2.5, 3.0, 3.5, and 4.0 eV. According to the definition of various resonant states [1] and the MRCI calculations for the electronic excited states of the neutral [14], the $^2A_1$ state lies lower in energy with respect to the corresponding excited state of the neutral, thus this resonant state is a single-particle shape resonance. Another electron transition $^1E \leftarrow {}^1A$ of the neutral was predicted to be around 7.0 eV [14], perhaps corresponding to the electron promotion to the LUMO + 3 orbital. In the photoabsorption experiments, a broad band with a maximum around 7.5 or 7.6 eV was also observed [22]. In the F^- production spectrum, the weak peak around 7.0 eV [5] should be related to a resonant

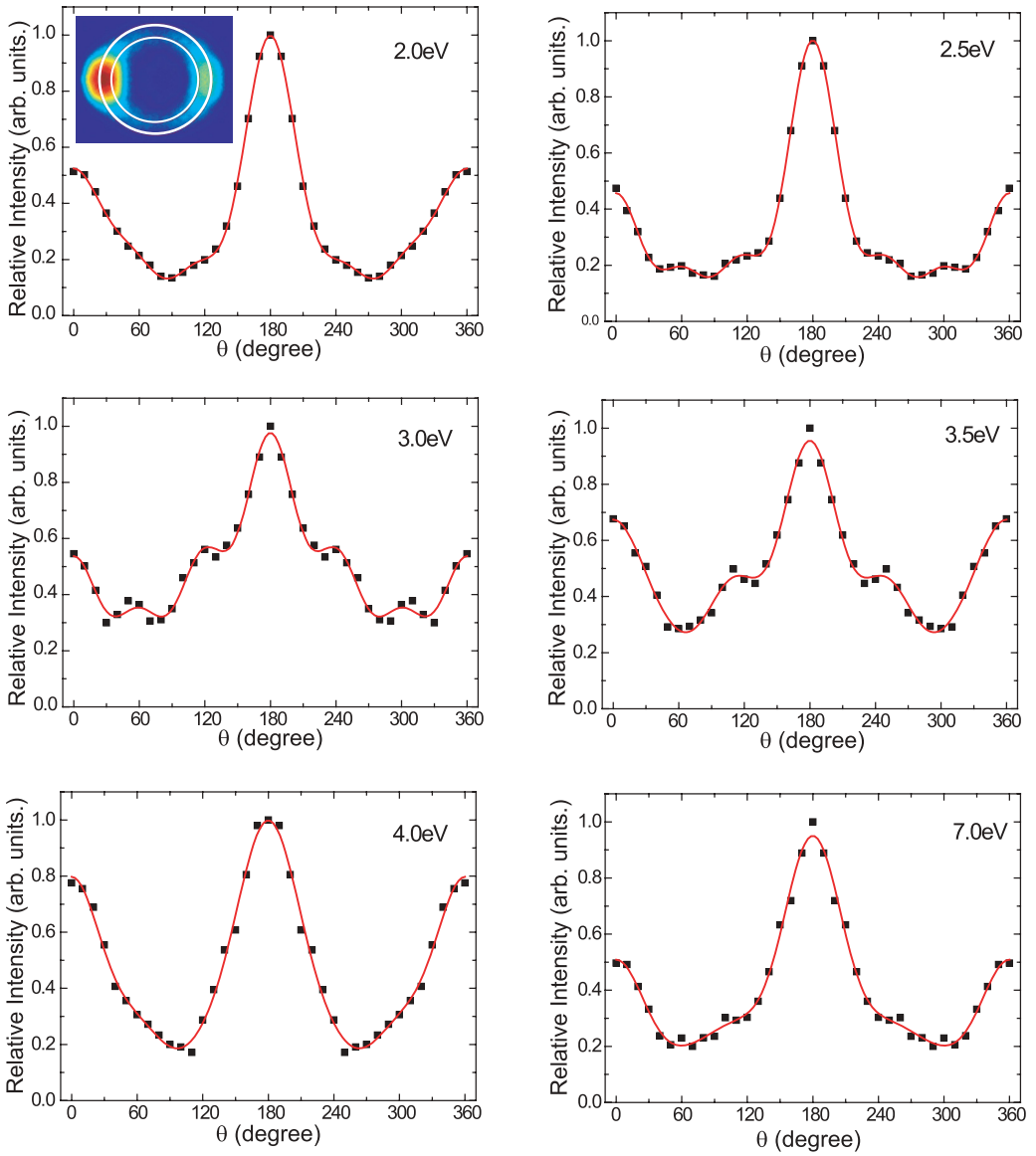

FIG. 3. (Color online) Angular distributions of the F^- fragment that are obtained by the integral of signals in the annular area (see the inside panel for the angular distribution at the electron attachment energy 2.0 eV). The annular areas correspond to the kinetic energy range of 0.63–1.03 eV at the electron attachment energy 2.0 eV; 0.68–1.08 eV at 2.5 eV; 0.60–1.0 eV at 3.0 and 3.5 eV; 0.48–0.88 eV at 4.0 eV; and 0.43–0.83 eV at 7.0 eV. The red lines represent the fitted results and the black dots are the experimental data.

state by the electron capture into the LUMO + 3 orbital. Usually, for a certain resonant state, its peak position observed in the anion yield spectrum is shifted to the higher energy in comparison with that in the electron transmission spectrum. Thus we suggest that the resonant state around 7.0 eV [5] should be assigned as another shape-resonant state.

To elucidate the angular distribution of anionic fragments produced in a DEA process, the formula of the differential cross section derived by Tronc *et al.* [23] is frequently used

$$\sigma_{\mathrm{DEA}} \propto \left| \sum_{l=\mu}^{\infty} i^l e^{i\delta_l} a(k)_{l\mu} Y_{l\mu}(\Omega) \right|^2, \qquad (1)$$

where k is the impinging electron wave vector and the impinging wave is further expressed with partial waves of different angular momenta l ($l \geqslant |\mu|$), Ω is the scattering direction of the fragment ion, $a(k)_{l\mu}$ is an energy-dependent expansion coefficient, and $Y_{l\mu}$ is a the spherical harmonics related to the initial (neutral) and final (resonant anion) states. $|\mu|$ equals $|\Lambda_f - \Lambda_i|$, representing the difference in the projection of the angular momentum along the internuclear axis for the neutral and resonant anion. In the formation of a resonant state, the different influences on each partial wave of the impinging electron by the interaction potential of the target result in the phase lags (δ_l) among these partial waves. Equation (1) is based on the pure resonant scattering-potential scattering approximation and originated from the theory of O'Malley and Taylor [24] and the symmetry arguments of Dunn [25]. Although this equation is only suitable for diatomic molecules, it still can be justified to use this diatomic approximation for polyatomic molecules if the dissociation is along the center of the mass axis of the molecule and the dominant portion of

the energy released going into the translational motion of the fragments is along the molecular axis [6]. Such a treatment also has been successfully applied in our previous work [8,9]. The process yielding F^- from $CFCl_3^-$ completely fits these conditions and can thus be treated as the dissociation of a quasidiatomic molecule (CCl_3–F^-). To obtain the angular distributions of the F^- fragment, we fitted the measured data (the points in Fig. 3) with Eq. (1) using a nonlinear least-squares fit. In practice, the summation of the finite partial wave terms together with the weight parameter $a_{l\mu}$ were used in the experimental data fitting [6,8,9,15]. Considering the C_{3v} symmetry of the neutral $CFCl_3$, the resonant state $^2A_1$ and the neutral ground-state $^1A_1$ lead to $|\mu| = 0$, and thus the basis functions Y_{l0} for the partial waves $l = 0$ (s), 1(p), 2 (d), and 3 (f) are used in this work. For the ^2E resonant state around 7.0 eV, different basis functions should be used. However, after the electron attachment to form the ^2E state, the molecular structure should be quickly distorted due to a Jahn-Teller effect. The C_{3v} symmetry is lowered to C_s symmetry, and this ^2E state will be split into $^2A'$ and $^2A''$ states. Since the partial waves defined with respect to the impinging electron vector k should be rotated into the dissociation frame on any potential surface of these one-dimensional representations (A' or A''), we will still have $|\mu| = 0$ along a pseudo-axis of the distorted $CFCl_3^-$. Therefore, the angular distributions obtained at all electron energies can be fitted with a common formula

$$\sigma_{\mathrm{DEA}} \propto |a_s Y_{00}(\theta) + i e^{i\delta_p} a_p Y_{10}(\theta) - e^{i\delta_d} a_d Y_{20}(\theta) - i e^{i\delta_f} a_f Y_{30}(\theta)|^2, \quad (2)$$

in which only the polar angle θ is considered for the central time-sliced images. The excellent correlations $R^2 \geqslant 0.98$ validate the conjecture mentioned above.

In Fig. 3, the angular distributions are obtained by the experimental data integrals for the annular area in each image in Fig. 1. The annular is selected to cover the highest intensities in the backward and forward directions. At the electron energy of 2.0 eV, the annular area corresponds to the F^- kinetic energy range of 0.63–1.03 eV; 0.68–1.08 eV at 2.5 eV; 0.60–1.0 eV at 3.0 and 3.5 eV; 0.48–0.88 eV at 4.0 eV; and 0.43–0.83 eV at 7.0 eV. As mentioned above, the relative intensities in the forward direction ($\theta \sim 0^\circ$ and 360°) increase from the low (2.0 eV) to the high (4.0 eV) electron energies. The fine structures in the sideward direction ($\theta = 60^\circ \sim 120^\circ$ and $240^\circ \sim 300^\circ$) are also observed at the electron energies 2.5, 3.0, and 3.5 eV. These fine structures disappear at 4.0 eV, but reappear somewhat at 7.0 eV. The different roles of various partial waves are listed in Table I. At the lowest electron energy 2.0 eV, the

TABLE I. The weighing ratios of partial wave contributions and the phase lags between them.

Attachment Energy	2.0 eV	2.5 eV	3.0 eV	3.5 eV	4.0 eV	7.0 eV
a_p/a_s	0.14	2.42	1.25	2.17	0.09	0.66
a_d/a_s	0.87	0.78	0.25	1.26	0.48	1.42
a_f/a_s	0.66	2.39	1.07	0.82	0.26	0.52
δ_p–δ_s (rad)	2.87	1.61	1.60	1.25	2.56	1.54
δ_d–δ_p (rad)	0.02	0.23	−0.48	−0.45	0.98	0.68
δ_f–δ_d (rad)	0.48	1.71	1.89	2.24	−0.14	0.19

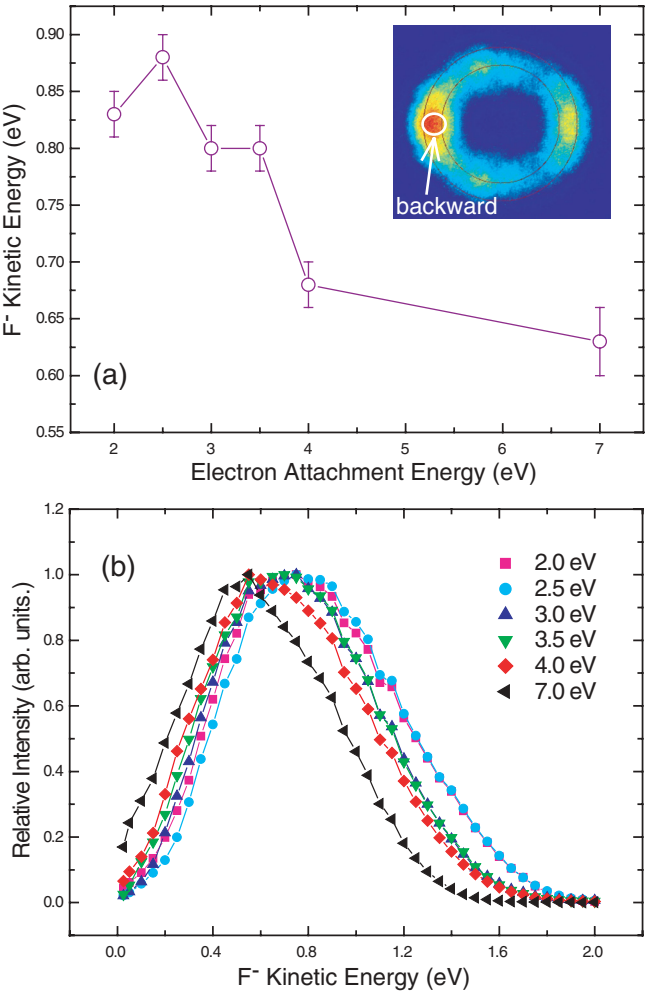

FIG. 4. (Color online) (a) Kinetic energy of the F^- fragment as a function of the electron attachment energy, only for the most intensive distribution in the backward direction ($\theta \sim 180^\circ$, shown as the inside panel). The statistic error is caused by the signal integral area. (b) The kinetic energy distributions of F^- obtained by the integrals over all polar angles.

contributions of the s, p, d, and f partial waves are in a ratio of 1: 0.14: 0.87: 0.66, indicating the predominant role of the s partial wave. With the increase of the electron energy, the partial waves with higher l (that is p, d, or f) become more abundant. As we expected, the larger angular momentum of the incident electron becomes dominant at the higher energy, thus its corresponding partial wave will contribute more to the DEA process. However, in contrast to this trend, the s partial wave contributions are predominant again at the higher electron energies, namely, the contributions of the s, p, d, f partial waves with the ratios of 1: 0.09: 0.48: 0.26 at 4.0 eV and 1: 0.66: 1.42: 0.52 at 7.0 eV. The phase lags between two partial waves represent the interference among the s, p, d, and f partial waves. Meanwhile, as shown in Fig. 1, the velocity values or kinetic energies of the F^- ion at 4.0 and 7.0 eV are smaller than those at the lower electron energies. This implies that the dissociative dynamics at higher electron energies should be different from that at lower electron energies.

As shown in Fig. 4(a), the F^- kinetic energies of the most intensive distributions in the backward direction ($\theta = 180^\circ$)

TABLE II. Energetics for various DEA channels of $CFCl_3$.

Dissociation channel	Calculations (eV)	Experimental Results (eV)
$CFCl_3 + e^- \rightarrow F^- + CCl_3\ (X\ ^2A_1)$	1.12	1.1 ± 0.2[a]
$CFCl_3 + e^- \rightarrow F^- + CCl_2 + Cl$	4.01	
$CFCl_3 + e^- \rightarrow F^- + CCl_3\ (^2A'')$	4.23	
$CFCl_3 + e^- \rightarrow F^- + CCl + Cl_2$	4.84	
$CFCl_3 + e^- \rightarrow F^- + C + Cl + Cl_2$	8.99	
$CFCl_3 + e^- \rightarrow Cl^- + CFCl_2\ (X\ ^2A')$	−0.36	∼0.0[b]

[a]Cited from Refs. [4,5].
[b]The peak position in the Cl^- yield curve [4,5].

are varying dramatically with the increase of the electron energy. Figure 4(b) exhibits the kinetic energy distributions of F^- obtained by the integrals over all polar angles. The relative intensity of the low kinetic energy partition (the left shoulder) decreases from an electron energy of 2.0 to 2.5 eV, but increases when the electron energy is higher; while with the increase of the electron energy, the relative intensity of the high kinetic energy partition (the right shoulder) decreases and its maxima shift to lower energy values. As listed in Table II, our thermochemical calculations indicate most dissociation paths are endothermic except for $e^- + CFCl_3 \rightarrow Cl^- + CCl_2F$. In the attachment energy range below 4.0 eV, the only dissociation channel accessible is $e^- + CFCl_3 \rightarrow F^- + CCl_3(X\ ^2A_1)$. Within momentum and energy conservations, the total kinetic energy release (E_k) can be estimated as [26]

$$E_k = E_k^i \frac{M}{m} - \frac{3}{2}RT\frac{m_i}{m}, \tag{3}$$

where E_k^i is the measured kinetic energy of the anionic fragment; M, m, and m_i are the masses of the parent molecule, neutral fragment (CCl_3), and anionic fragment (F^-), respectively; R is the gas constant; and T is the gas-sample temperature. Here only the kinetic energies of CCl_3 ($X\ ^2A_1$) in the forward direction and the F^- fragment in the backward direction are considered in Eq. (3). The maximal value of E_k ($E_k{}^{max}$) can be derived directly as the difference between the electron attachment energy and the dissociation threshold. Table III clearly indicates that the E_k values are much smaller than $E_k{}^{max}$, except for the case at 2.0 eV. The result of $E_k{}^{max} > E_k$ at 2.0 eV can be interpreted by the comparably large energy spread of the electron beam (FWHM ∼ 0.5 eV) in the present experiment. At the lower attachment energies

TABLE III. Total kinetic energy release (E_k) in the two-body dissociation $CFCl_3 + e^- \rightarrow F^- + CCl_3\ (X\ ^2A_1)$.

Attachment Energy (eV)[a]	E_k (eV)[a]	$E_k{}^{max}$ (eV)[b]	Attachment Energy (eV)[c]	E_k (eV)[c]
2.0	0.96	0.88	1.9	0.33
2.5	1.02	1.38	2.5	0.41
3.0	0.92	1.88	3.1	0.65
3.5	0.92	2.38	3.7	0.82
4.0	0.78	2.88	4.1	0.91

[a]The present measurements.
[b]From the present thermochemical calculations.
[c]Estimated from Ref. [5].

2.0 and 2.5 eV, the excess energy is efficiently converted into kinetic energy of the fragments, but much less so at the higher energies (3.0–4.0 eV). At the higher attachment energies, a considerable part of the excess energy should be transferred into internal excitation of the CCl_3 fragment. On the other hand, the E_k values estimated from Ref. [5] are also listed in Table III for comparison. In that work, the kinetic energy of F^- was calculated on the basis of the ion arriving time difference in the time-of-flight scheme [5]. Since the ion lenses used in that experiment [5] were not precisely designed for ion velocity imaging, the results of the F^- kinetic energy cannot be simply compared with the present values. Whatever, the E_k values from Ref. [5] and ours are conformably lower than the $E_k{}^{max}$ values.

At the attachment energy 7.0 eV, the present thermochemical calculations (see Table II) indicate that other dissociation channels, $e^- + CFCl_3 \rightarrow F^- + CCl_3(^2A'')$ (threshold ∼ 4.23 eV), $e^- + CFCl_3 \rightarrow F^- + CCl_2 + Cl$ (threshold ∼ 4.01 eV), and $e^- + CFCl_3 \rightarrow F^- + CCl + Cl_2$ (threshold ∼ 4.84 eV), may be accessed. In the two-body dissociation with the fragment CCl_3 at the electronically excited state $^2A''$, the total kinetic energy E_k of the two fragments is about 0.73 eV, thus the CCl_3 ($^2A''$) should be populated in the rovibrational excited states 2.04 eV higher than its rovibrational ground state. By collection and analysis of the photoemission of CCl_3 decaying from the $^2A''$ state to the ground state $^2A_1$, the population of the rovibrational excited states of the electronic state $^2A''$ can be further determined. Alternatively, this highly rovibrationally excited CCl_3 ($^2A''$) may also be subsequently decomposed to $CCl_2 + Cl$ or $CCl + Cl_2$. It is more interesting that these direct or indirect three-body dissociations may result in the much lower kinetic energy of the F^- fragment by the more efficient transfer of the excess energy into the kinetic energy. Four-body fragmentation $e^- + CFCl_3 \rightarrow F^- + C + Cl + Cl_2$(8.99 eV) is beyond the present study due to its even higher energetic threshold. Since Eq. (3) is unsuitable for many-body fragmentations and the present experimental technique is unfeasible to identify the preference of the high-threshold dissociation paths, we cannot provide more information about the dissociation dynamics at such a high electron energy.

IV. CONCLUSION

Low-energy electron dissociative attachment to $CFCl_3$ is studied by using our developed time-sliced anion velocity imaging apparatus. The time-sliced velocity images of F^-

anionic fragment recorded at the different electron attachment energies indicate image pattern evolutions. To interpret the angular distributions of F^-, two one-particle shape-resonant states $^2A_1$ and ^2E of $CFCl_3{}^-$ are proposed and deserve further computational study using sophisticated quantum scattering theory. The present thermochemistry calculations indicate that four dissociation channels may be involved in the present experiments, moreover, with the increase of the electron attachment energy, more and more excess energy could be transferred into the internal excitation of CCl_3. Possible three-body dissociation is discussed for the dramatic reduction of the kinetic energy of F^- fragment observed at the higher attachment energies.

ACKNOWLEDGMENTS

This work is supported by MOST (Grant No. 2013CB834602), NSFC (Grant No. 21273213), and FRFCU.

[1] L. G. Christophorou, *Electron Molecule Interactions and Their Applications* (Academic, New York, 1984).
[2] J. Randell, J.-P. Ziesel, S. L. Lunt, G. Mrotzek, and D. Field, J. Phys. B **26**, 3423 (1993).
[3] K. Aflatooni and P. D. Burrow, Int. J. Mass Spectrom. **205**, 149 (2001).
[4] E. Illenberger, H.-U. Scheunemann, and H. Baumgärtel, Chem. Phys. **37**, 21 (1979).
[5] E. Illengerger, Ber. Bunsenges. Phys. Chem. **86**, 252 (1982).
[6] F. H. Ómarsson, O. Ingólfsson, N. J. Mason, and E. Krishnakumar, Eur. Phys. J. D **66**, 51 (2012).
[7] H. Adaniya, B. Rudek, T. Osipov, D. J. Haxton, T. Weber, T. N. Rescigno, C. W. McCurdy, and A. Belkacem, Phys. Rev. Lett. **103**, 233201 (2009).
[8] B. Wu, L. Xia, Y.-F. Wang, H.-K. Li, X.-J. Zeng, and S. X. Tian, Phys. Rev. A **85**, 052709 (2012).
[9] L. Xia, B. Wu, H.-K. Li, X.-J. Zeng, and S. X. Tian, J. Chem. Phys. **137**, 151102 (2012).
[10] A. Chutjian, Phys. Rev. Lett. **46**, 1511 (1981); **48**, 289 (1982).
[11] R. K. Jones, J. Chem. Phys. **84**, 813 (1984).
[12] M. Meitina and E. Illenberger, J. Phys. Chem. **98**, 6601 (1994).
[13] D. Klar, M.-W. Ruf, I. I. Fabrikant, and H. Hotop, J. Phys. B **34**, 3855 (2001).
[14] S. D. Peyerimhoff and R. J. Buenker, Chem. Phys. Lett. **65**, 434 (1979).
[15] D. Nandi, V. S. Prabhudesai, B. M. Nestmann, and E. Krishnakumar, Phys. Chem. Chem. Phys. **13**, 1542 (2011).
[16] B. Wu, L. Xia, H.-K. Li, X.-J. Zeng, and S. X. Tian, Rev. Sci. Instrum. **83**, 013108 (2012).
[17] A. K. Wilson, T. vanMourik, and T. H. Dunning, J. Mol. Struct. (THEOCHEM) **388**, 339 (1996); T. H. Dunning, Jr., K. A. Peterson, and A. K. Wilson, J. Chem. Phys. **114**, 9244 (2002).
[18] K. A. Peterson and T. H. Dunning, J. Chem. Phys. **117**, 10548 (2002).
[19] M. Douglas and N. M. Kroll, Ann. Phys. (NY) **82**, 89 (1974); G. Jansen and B. A. Hess, Phys. Rev. A **39**, 6016 (1989).
[20] N. B. Balabanov and K. A. Peterson, J. Chem. Phys. **123**, 064107 (2005); W. A. de Jong, R. J. Harrison, and D. A. Dixon, *ibid.* **114**, 48 (2001).
[21] H. J. Werner, P. J. Knowles, M. Schütz *et al.*, MOLPRO is a package of *ab initio* programs.
[22] J. Doucet, P. Sauvageau, and C. Sandorfy, J. Chem. Phys. **58**, 3708 (1973); R. H. Huebner, D. L. Bushnell, R. J. Celotta, S. R. Mielczarek, and C. E. Kuyatt, Nature (London) **257**, 376 (1975).
[23] M. Tronc, C. Schermann, R. I. Hall, and F. Fiquet-Fayard, J. Phys. B **10**, 305 (1977).
[24] T. F. O'Malley and H. S. Taylor, Phys. Rev. **176**, 207 (1968).
[25] G. H. Dunn, Phys. Rev. Lett. **8**, 62 (1962).
[26] M. A. Haney and J. L. Franklin, J. Chem. Phys. **48**, 4093 (1968).